Construction of catalytic ozonation synergistic photo-self-Fenton system and analysis of synergistic catalysis and reaction mechanism activated by modified carbon nitride

Benjie Zhu [a], Yuting Wang [a], Chenxing Li [a], Fei Gao [a], Fang Liu [a,*], Guofei Jiang [a,b], Huaqing Zhang [c], Xiaoguang Duan [d,*]

[a] College of Chemistry and Chemical Engineering, China University of Petroleum, Qingdao 266580, China
[b] School of Chemistry and Chemical Engineering, Heze University, Heze 274015, China
[c] College of Science, China University of Petroleum, Qingdao 266580, China
[d] School of Chemical Engineering and Advanced Materials, The University of Adelaide, Adelaide, SA 5005, Australia

ARTICLE INFO

ABSTRACT

This study developed multifunctional Cl, S doped carbon nitride nanotube composite molybdenum disulfide with S vacancy ($CN_{Cl/S}/MoS_{2v}$) for catalytic ozonation synergistic photo-self-Fenton (COP_{SF}) reactions. Through characterization, DFT simulation and machine learning (ML) methods, we reveal the functions and mechanisms of heteroatom dopants, defect sites, and built-in electric fields on promoting photogenerated charge carrier migration, transfer, as well as optimizing local/global properties for spontaneously promoted photocatalysis and heterogeneous ozone activation. As a result, $CN_{Cl/S}/MoS_{2v}$-COP_{SF} system exhibited greatly enhanced synergistic activity compared with individual systems with a synergistic factor of 1.35. The oxidation synergy stems from the collaborations of photo-induced production H_2O_2, heterogeneous activation of O_3, as well as their interplays to evolve more reactive species such as $*O$, $^\bullet OH$, $O_2^{\bullet-}$. Thus, this work provides mechanistic insights into the coupled advanced oxidation systems with to boost the pollutant degradation kinetics.

1. Introduction

The increasing water consumption and complex chemical use in petrochemical industry have generated a large amount of wastewater, which has impacted traditional water treatment processes and exacerbated the shortage of water resources [1–3]. The presence of refractory organic pollutants, especially emerging contaminants (ECs) in petrochemical wastewater, has become a major obstacle to the improvement of wastewater treatment standards and reuse of water resource [4,5]. For the treatment of petrochemical wastewater, advanced oxidation process (AOP) is one of the most effective technologies due to its flexibility, controllability, and strong mineralization ability [6,7]. Single AOP such as photocatalysis (PO), Fenton, and catalytic ozonation (CO) have limitations such as limited reaction rate, potential secondary pollution, low energy utilization efficiency, and poor adaptability to complex water quality [8–10]. Constructing synergistic AOP (SAOP) through developing multifunctional catalysts is an effective way to combine collaborative control of complex wastewater and operating

modes with high efficiency and low chemical consumption.

In previous work, we demonstrated that, the catalytic ozonation synergistic photocatalytic (COP) system existed multi-path activation of O_3 by alkaline, catalyst, and photo-generated elections (e^-) [11]. Although COP system reduces the dependence of O_3 activation on pH in CO and improves photo-electron utilization efficiency in PO, the system cannot effectively overcome the limitation that the reaction rate of O_3 $+OH^- \rightarrow HO_2^-$ in CO activation reaction is much slower than other reactive oxygen species (ROS) such as $HO_2+O_3 \rightarrow ^\bullet OH$ or $O_2^{\bullet-}$ [12]. The H_2O_2 in Fenton process can decompose/ionize to produce HO_2^-, which quickly participates in the ROS reaction in CO and reduces the impact of the above limiting steps. However, additional H_2O_2 increases the cost and makes the operating conditions more complex. Surprisingly, the photo-self-Fenton (P_{SF}) technology has brought a turning point to this bottleneck issue [13]. P_{SF} process can simultaneously produce photo-e^- and H_2O_2 simultaneously with clean energy and no secondary pollution [14]. Although H_2O_2 have longer half-life compared to free radicals [15], simultaneously efficient H_2O_2 production and activation in one P_{SF}

---

system is still challenging. The synergistic reaction between CO and P_{SF} is a possible way to promote the efficient activation of O_3 and H_2O_2, and treat petrochemical wastewater with clean energy and high efficiency.

However, the synergistic mechanism between CO and P_{SF} and the coupled system has been less reported. Based on the catalytic potential of carbon nitride for both CO and P_{SF}, as well as its environmental friendliness [16,17], carbon nitride is a promising bifunctional catalyst. And its structure and activity can be regulated through various modification methods, to explore the potential synergistic catalysis and reaction mechanisms when coordinating CO and P_{SF} processes. By adjusting the morphology [18] and doping elements [19], the photo-generated carriers migration, electron cloud distribution, and band structure of carbon nitride can be finely tuned. There are multiple e^- transfer pathways involved in the synergistic reaction process, such as participating in the production of H_2O_2, promoting the multiple pathways activation of O_3 (e^-, H_2O_2, catalyst, OH^-), and participating in free radical reactions. In order to further increase the production of active species, n-type semiconductor molybdenum disulfide [20] is introduced through heterojunction engineering to promote photo charge carrier production and transport efficiency [21,22]. In addition, molybdenum disulfide has both CO and P_{SF} potentials and is easy to form S vacancy in the preparation process to enhance the photocatalysis and the intrinsic heterogeneous activity [23].

This study aims to construct catalytic ozonation synergistic photo-self-Fenton (COP_{SF}) system, and conduct in-depth exploration of carrier migration and its synergistic catalytic mechanism, transformation behaviors of active species during synergistic reactions, and the correlation between descriptors and local properties. We developed Cl, S doped carbon nitride nanotube composite molybdenum disulfide with S vacancy ($CN_{Cl/S}/MoS_{2v}$) to drive synergistic catalysis and water decontamination. The applicability of different machine learning models in predicting complex synergistic systems is also explored. This study has guiding significance in the fields of efficient treatment of petrochemical wastewater and in-depth exploration of the synergistic mechanism in complex systems. This study would particularly shed light on efficient treatment of petrochemical wastewater by the COP_{SF} system with mechanistic insights into interplays of different catalytic pathways.

2. Materials and methods

2.1. Chemicals and catalysts

$CN_{Cl/S}/MoS_{2v}$ heterojunction is prepared through post-recombination method. Melamine and cyanuric acid are used as raw materials. Ammonium chloride and thiourea are used as Cl, S dopants, $CN_{Cl/S}$ is prepared by a hydrothermal self-repairing method. With molybdenum trioxide and Potassium thiocyanate as raw materials, MoS_{2v} is prepared by hydrothermal method. Details are presented in Text S1 in the Supplementary Data.

2.2. Activity measurements and analytical methods

The activity measurements are conducted in a sealed quartz container with cooling circulating water jacket (100 ML, 25 °C). The light source is 300 W xenon lamp with 420 nm filter. The ozone source is SW-112 ozone generator (20 ML/min). Unless otherwise specified, the catalyst dosage is 0.5 g/L and the target pollutant concentration is 20 mg/L. Analytical details are provided in Text S2. The actual petrochemical wastewater selected are low salinity-low COD petrochemical wastewater (LPW) and high salinity-high COD petrochemical wastewater (HPW). The water sampling points and water quality of six types of samples are shown in Scheme S1, S2 and Table S1.

2.3. Computational methods

The calculation of descriptors DMOL3 package based on density

functional theory is implemented in Materials Studio. The ML scheme is performed by using common models like Feedforward Neural Network (FNN), Naive Bayesian (NB), Regression Tree (RT), Random Forest (RF) and eXtreme Gradient Boosting (XGBoost), which are implemented in python. Detailed implementations are provided in Text S3.

3. Results and discussion

3.1. Enhanced activity and synergistic effect of $CN_{Cl/S}/MoS_{2v}$-COP_{SF} system

According to Fig. 1a-c, the degradation rate of p-nitrophenol (PNP) in $CN_{Cl/S}/MoS_{2v}$-P_{SF}, $CN_{Cl/S}/MoS_{2v}$-CO and $CN_{Cl/S}/MoS_{2v}$-COP_{SF} system can reach 12.1%, 96.4%, and 99.2% in 30 min, which is 3.7%, 12.8%, and 8.9% higher than that in $CN_{Cl/S}$-P_{SF}, $CN_{Cl/S}$-CO and $CN_{Cl/S}$-COP_{SF} system, respectively. The kinetic processes in P_{SF} and CO, COP_{SF} systems are generally summarized as first-order (Eq. 1) and second-order kinetic (Eq. 2) to analyze the reaction activities of different systems [24]. As reported, the direct reaction rate of O_3 and PNP is low [25], so Eqs. 1 and 2 both can be simplified as pseudo first-order reaction kinetic equation (Eq. 3 and Fig. 1b). When using $CN_{Cl/S}/MoS_{2v}$ as the catalyst, the reaction rate of P_{SF}, CO and COP_{SF} systems are 0.0067, 012 and 0.18 min^{-1}, which is 1.3, 1.7 and 2.0 times higher than the system catalyzed by $CN_{Cl/S}$, respectively. The $CN_{Cl/S}/MoS_{2v}$-based COP_{SF} system also well outperformed other reported ozonation systems in Table S2. It is worth noting that $CN_{Cl/S}/MoS_{2v}$-P_{SF} system has slight improvement for PNP degradation, but its generation rate of H_2O_2 has been significantly improved (293.1 $\mu mol \bullet g^{-1} \bullet h^{-1}$), which is 3.4 times that of $CN_{Cl/S}$-P_{SF} system (Fig. 1d). This may be because $CN_{Cl/S}/MoS_{2v}$-P_{SF} system cannot fully activate H_2O_2 to produce ROS such as $^{\bullet}OH$ (2.80 V), and thus inactivated H_2O_2 (1.77 V) was not capable of degrading PNP. Nonetheless, the enhanced catalytic ability of P_{SF}, CO, and the production ability of H_2O_2 are all beneficial for the synergy and activity of COP_{SF} system.

$$\frac{d[C]}{dt} = -k_{ROS,C}[ROS][C] \tag{1}$$

$$\frac{d[C]}{dt} = -(k_{O_3,C}[O_3][C] + k_{ROS,C}[ROS][C]) \tag{2}$$

$$-\ln\frac{C}{C_0} = kt \tag{3}$$

where [C], [O_3] and [ROS] is the concentration ($mg \bullet L^{-1}$) of PNP, O_3 and ROS, respectively. $k_{O_3,C}$ and $k_{ROS,C}$ is the reaction rate constant (min^{-1}) of PNP with O_3 and ROS, respectively. C and C_0 is C are the PNP concentration ($mg \bullet L^{-1}$) at time t and 0 min

The enhanced activity of COP_{SF} system is further demonstrated by comparing the degradation and mineralization rates of PNP in $CN_{Cl/S}/MoS_{2v}$-P_{SF}, O_3, $CN_{Cl/S}/MoS_{2v}$-CO, and $CN_{Cl/S}/MoS_{2v}$-COP_{SF} systems. The degradation efficiency of PNP by $CN_{Cl/S}/MoS_{2v}$-COP_{SF} system can reach 96.8% in 20 min, which is 91.5%, 89.1%, and 16.5% higher than $CN_{Cl/S}/MoS_{2v}$-P_{SF}, O_3 and $CN_{Cl/S}/MoS_{2v}$-CO system, respectively. And the degradation rate of PNP by $CN_{Cl/S}/MoS_{2v}$-COP_{SF} system can exceed 99% in 30 min. Furthermore, the mineralization effect of PNP is evaluated through TOC removal (Fig. 5c), reaching 75.2% in 120 min in $CN_{Cl/S}/MoS_{2v}$-COP_{SF} system, that is 44.1%, 36.0%, and 13.8% higher than $CN_{Cl/S}/MoS_{2v}$-P_{SF}, O_3, and $CN_{Cl/S}/MoS_{2v}$-CO system, respectively.

The synergistic effect of P_{SF} and CO on the generation and decomposition of H_2O_2 in COP_{SF} system is analyzed based on the dynamical model. According to Fig. 2a and Table S3, traditional O_3 reaction rate is mainly limited by the generation step of HO_2^- (70 $M^{-1} \bullet s^{-1}$). Once HO_2^- is generated, it will participate in the ROS generation in the COP_{SF} system at a high reaction rate of 10^6-10^{10} $M^{-1} \bullet s^{-1}$. Additionally, H_2O_2 can react with various active components to generate ROS or be ionized to produce HO_2^- ($H_2O_2 \rightleftarrows HO_2^- + H^+$) in the COP_{SF} system. The coupled system of
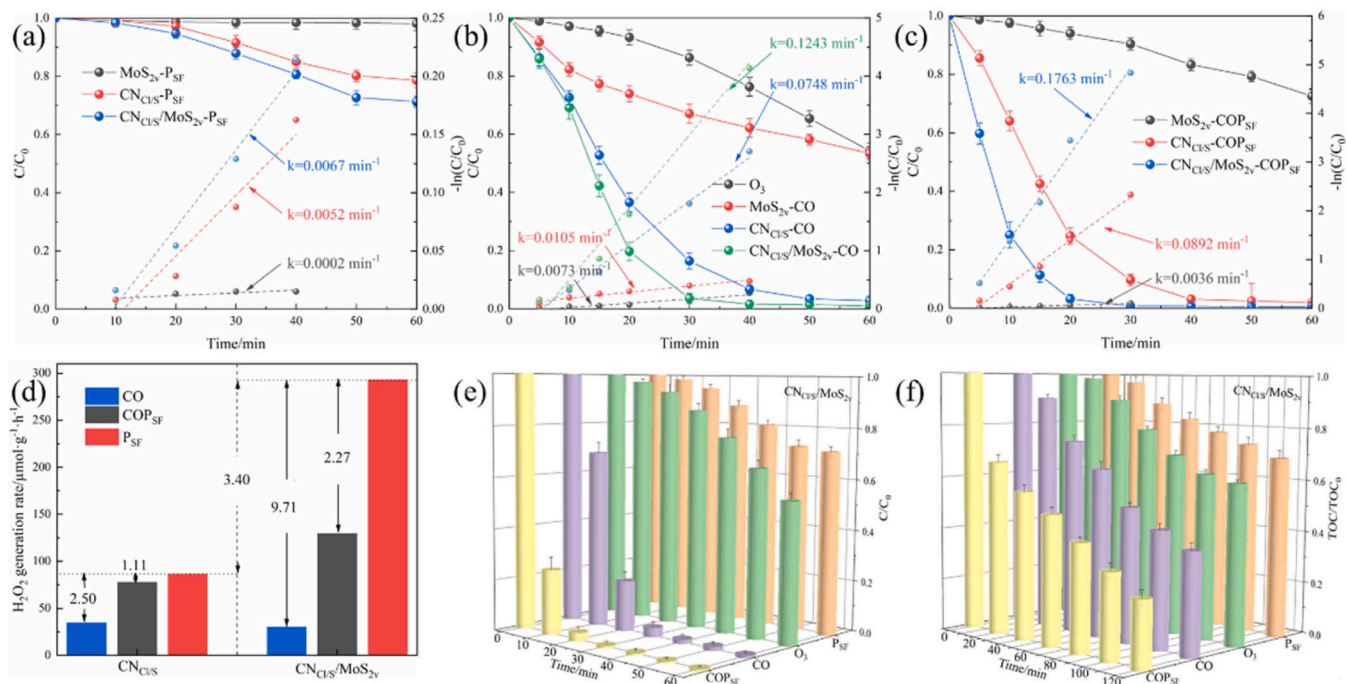
Fig. 1. The degradation efficiency and kinetic constant (k/min^{-1}) of PNP in (a) P_{SF}, (b) CO and (c) COP_{SF} system. Comparison of (d) H_2O_2 generation rate in CO, COP_{SF} and P_{SF} systems. (e) PNP degradation rates and (f) mineralization rate in $CN_{Cl/S}/MoS_{2v}$-P_{SF}, O_3, $CN_{Cl/S}/MoS_{2v}$-CO and $CN_{Cl/S}/MoS_{2v}$-COP_{SF} systems (the concentration of catalyst and PNP is 0.5 g/L and 20 mg/L, light source is 300 W xenon lamp, 15 A, ozone concentration is 10 mg/L, 20 ML/min).
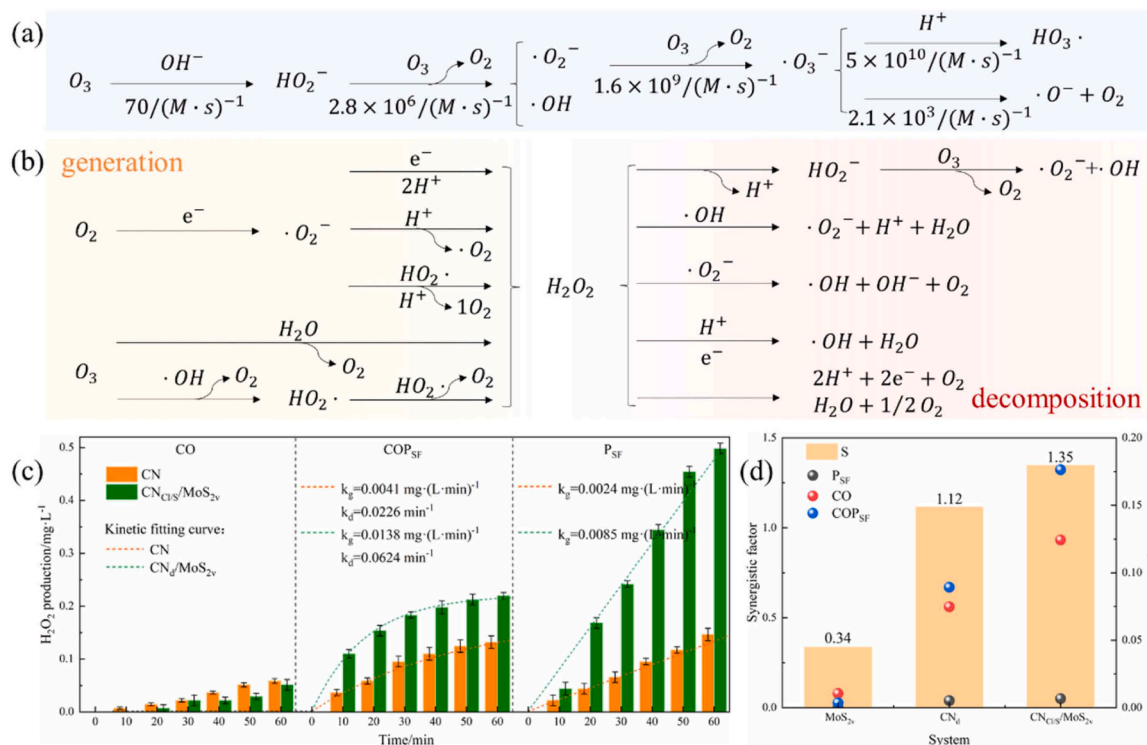

Fig. 2. (a) Traditional O_3 reaction equation and rate constant. (b) Possible H_2O_2 generation and decomposition reactions involved in COP_{SF} system. (c) H_2O_2 production and kinetic fitting curve in CO, COP_{SF} and P_{SF} systems (the concentration of catalyst is 0.5 g/L, light source is 300 W xenon lamp, 15 A, ozone concentration is 10 mg/L, 20 ML/min). (d) k values in different reaction systems (scatter plot) and synergistic factors in COP_{SF} system (bar chart).

COP_{SF} involves H_2O_2 formation reactions like one-step or multi-step $2e^-$ oxygen reduction reaction (ORR), ROS, or catalyst surface e^- transfer reaction (Table S4). COP_{SF} also involves multi-path consumption reactions of H_2O_2, such as Haber Weiss reaction with free radicals [26],

redox with H^+, e^-, etc., and free radical formation reaction with O_3 reaction chain (Table S5). It is necessary to analyze the complex H_2O_2 generation and decomposition processes (Fig. 2b) by constructing dynamic models.
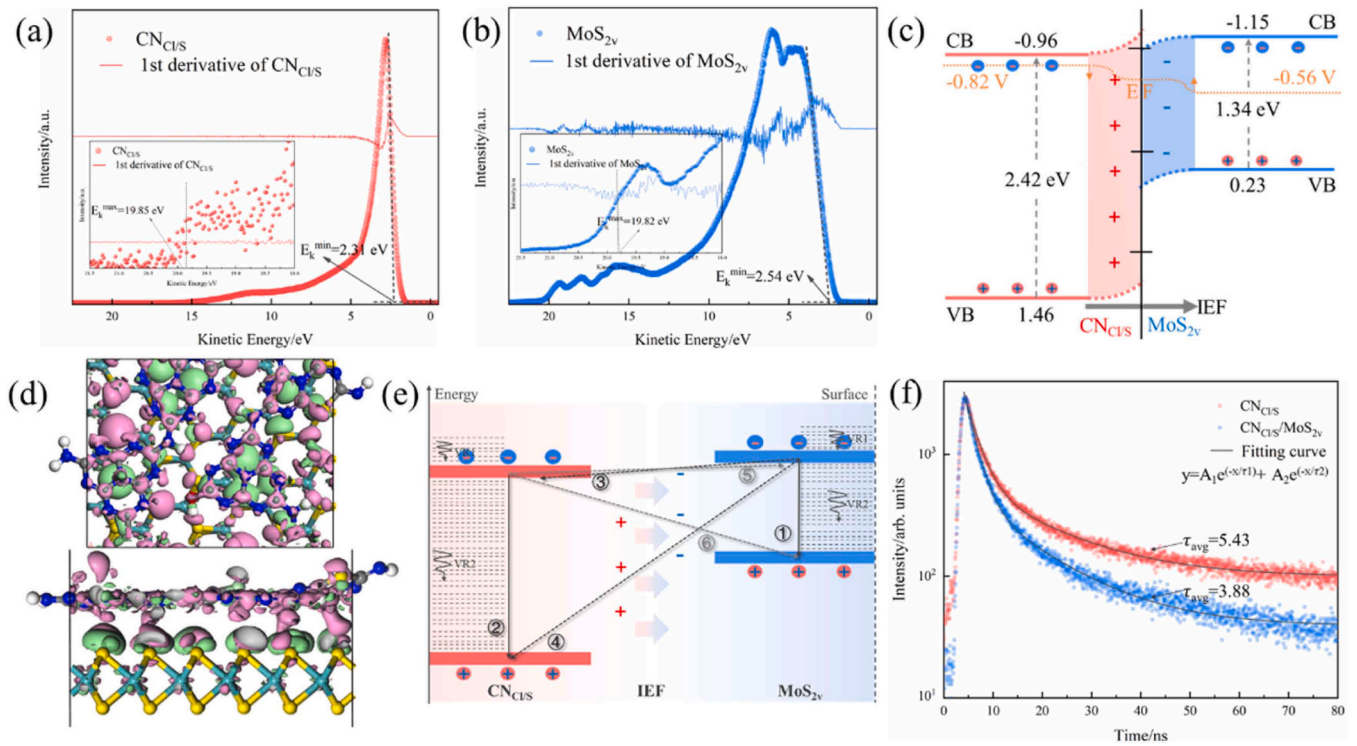
Fig. 3. UPS spectra of (a) $CN_{Cl/S}$ and (b) MoS_{2v}. (c) Schematic diagram of energy bands under the influence of IEF. (d) Differential charge of $CN_{Cl/S}/MoS_{2v}$ (above: top view, below: side view; pink: depletion layer, green: accumulation layer). (e) Possible electron migration path in $CN_{Cl/S}/MoS_{2v}$ after excitation by sunlight, VR_1 and VR_2 represent relaxation towards CB bottom and lattice atoms (commonly seen in lattice defects), respectively. (f) TRPL spectra of $CN_{Cl/S}$ and $CN_{Cl/S}/MoS_{2v}$. τ_{avg} represents the average photogenerated carrier decay time.
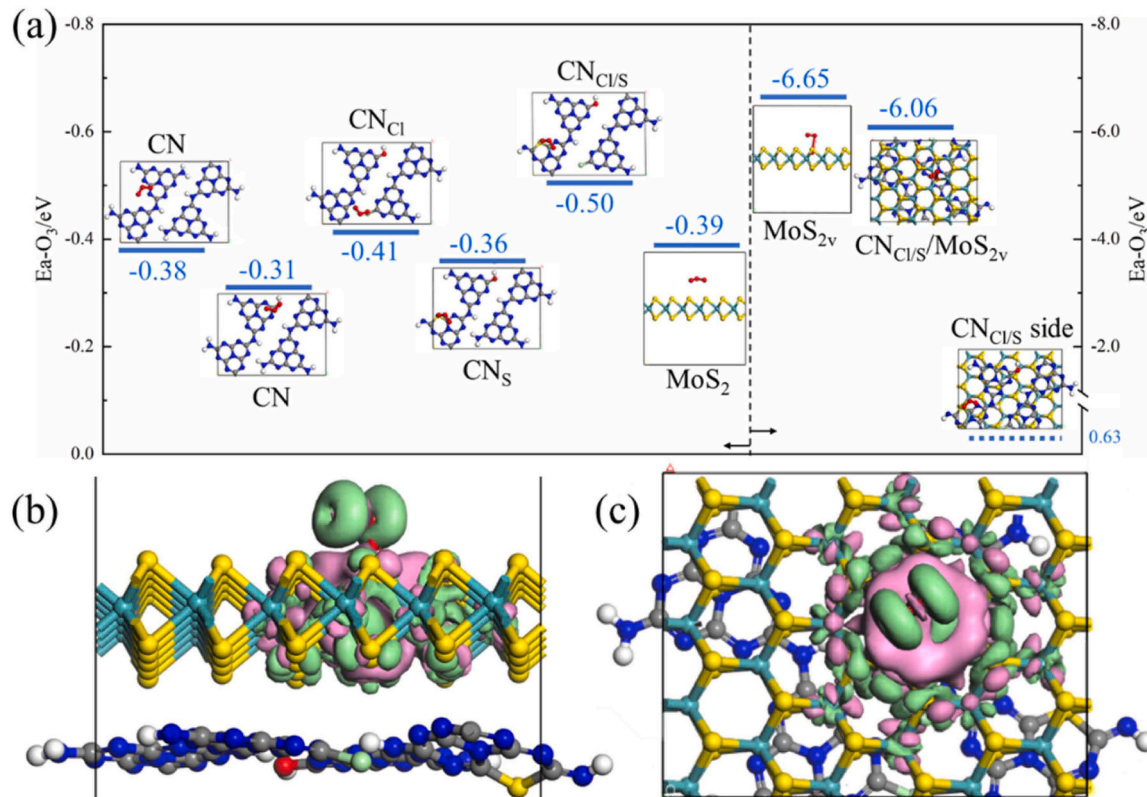

Fig. 4. (a) The influence of element doping, S vacancy and heterojunction engineering on $EA-O_3$. Differential charge distribution map of $CN_{Cl/S}/MoS_{2v}$ on O_3 adsorbed state: (b) side view, (c) top view (pink: depletion layer, green: accumulation layer).
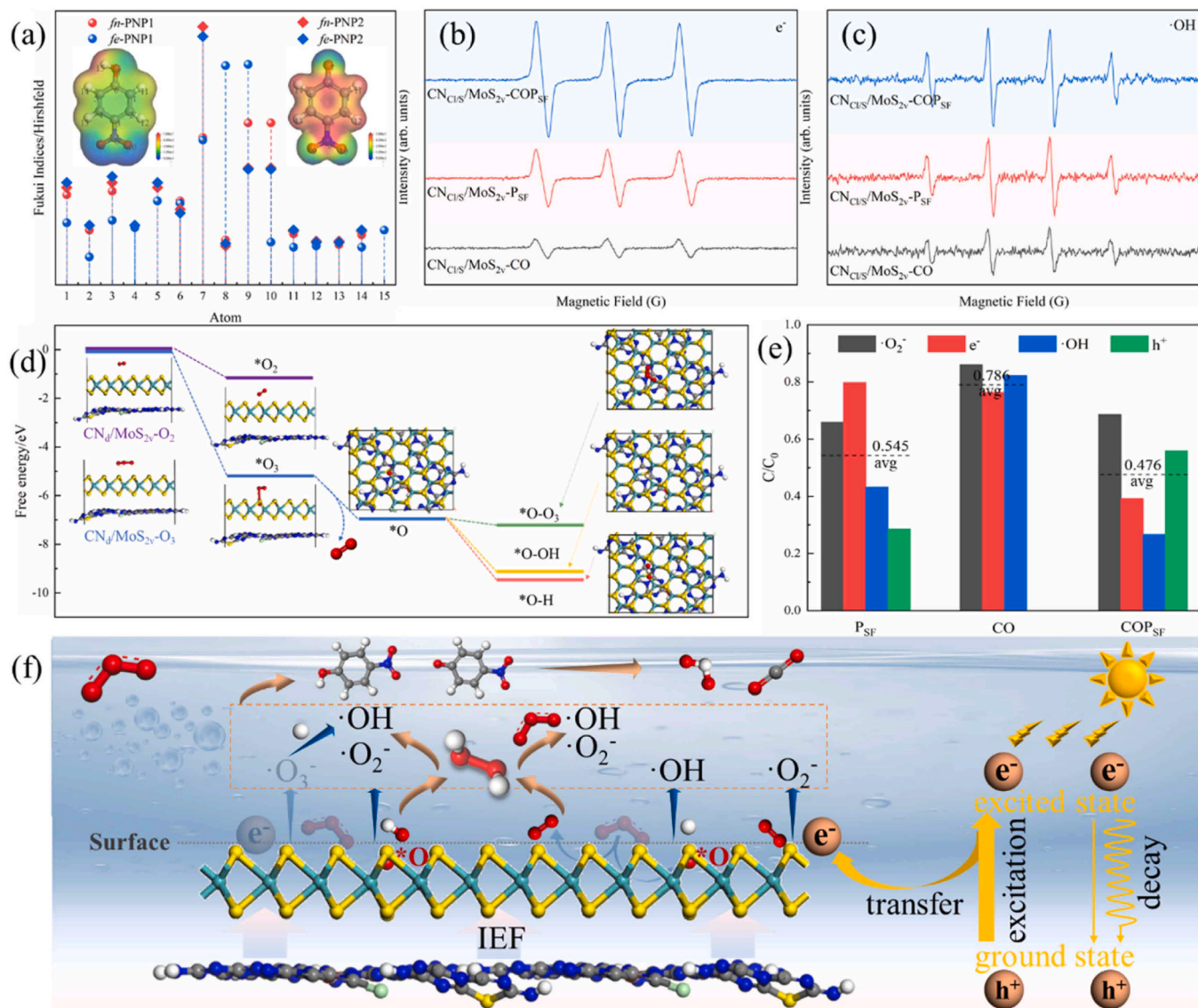
Fig. 5. (a) Fukui indices of elements in molecular state (PNP1) and ionic state (PNP2). Comparison of ESR spectra (10 min) of (b) $^\bullet$OH and (c) e^- in different systems. (d) Changes in free energy of different components reacting on the surface of $CN_{Cl/S}/MoS_{2v}$. (e) Quenching experiments for $O_2^{\bullet-}$, e^-, $^\bullet$OH and h^+ (comparison of degradation results at 60 min). (f) Schematic diagram of active species transfer and synergistic reaction in $CN_{Cl/S}/MoS_{2v}$-COP_{SF} system.

Thus, the inductive equation of H_2O_2 multiple pathways (Eq. 4) is proposed to simplify its kinetic analysis process. The concentrations of O_2, O_3 and ROS that involved in H_2O_2 generation are relatively low [27], and ROS is often regarded as a steady-state balance in kinetic models [12]. Thus, Eq. 4 can be simplified to Eq. 5.

$$v_{H_2O_2} = \sum_1^i k_{gi} \bullet [G_i] - \sum_1^j k_{dj} \bullet [D_j][H_2O_2] \quad (4)$$

$$\frac{d[H_2O_2]}{dt} = k_g - k_d[H_2O_2] \quad (5)$$

where $\sum_1^i k_{gi} \bullet [G_i]$ is the sum of the H_2O_2 generation kinetic rate, $\sum_1^j k_{dj} \bullet [D_j][H_2O_2]$ is the sum of H_2O_2 decomposition kinetic rate, k_g and k_d are the approximate generation and decomposition kinetic constants of H_2O_2, respectively.

The relationship Eq. 6 between $[H_2O_2]$ and t is obtained by analyzing Eq. 5, then k_g and k_d can be obtained through curve fitting. When k_g is much greater or much less than k_d, Eq. 5 can be simplified and analyzed to obtain Eq. 7 and Eq. 8, respectively.

$$[H_2O_2] = \frac{k_g}{k_d} \bullet (1 - e^{-k_d \bullet t}) \quad (6)$$

$$[H_2O_2]_G = k_g \bullet t \quad (7)$$

$$[H_2O_2]_D = [H_2O_2]_G \bullet e^{-k_d \bullet t} \quad (8)$$

The fitting result of H_2O_2 reaction process is shown in Fig. 2c and Table S6. The P_{SF} system is more in line with Eq. 7, where the H_2O_2 generation kinetic rate is much greater than decomposition kinetic rate. This also implies that although P_{SF} process can spontaneously generate H_2O_2, the activation efficiency of H_2O_2 is low, resulting in inconspicuous enhancement of PNP degradation rate in $CN_{Cl/S}/MoS_{2v}$-P_{SF} system (Fig. 1a). COP_{SF} system is fit better in Eq. 3. As a synergistic system with multiple active components, the COP_{SF} system not only provides a favorable environment for H_2O_2 generation (Table S4), but also provides multiple pathways for the activation of H_2O_2 and O_3 (Fig. 2a, b). According to the fitting results, although $CN_{Cl/S}/MoS_{2v}$-COP_{SF} system has a lower H_2O_2 generation rate (129.31 $\mu mol \bullet g^{-1} \bullet h^{-1}$, Fig. 1d), it has 1.6 times greater k_g (0.0138 min^{-1}) than $CN_{Cl/S}/MoS_{2v}$-P_{SF} system

(0.0085 min^{-1}). Moreover, the calculation of synergistic factors (S, Eq. S1) further indicates the synergistic effect of CO and P_{SF} in COP_{SF} system (Fig. 2d). The S of $CN_{Cl/S}$/MoS_{2v}-COP_{SF} system is 1.35, which is significantly stronger than the synergistic effect of P_{SF} and CO in $CN_{Cl/S}$-COP_{SF} system (S=1.12). This significant synergistic effect is closely related to the synergy of P_{SF} and CO in $CN_{Cl/S}$/MoS_{2v}-COP_{SF} system, as well as synergistic reaction activity of active species such as H_2O_2 and O_3.

3.2. Mechanism of carrier migration and synergistic catalytic activity in $CN_{Cl/S}$/MoS_{2v}-COP_{SF} system

$CN_{Cl/S}$/MoS_{2v} with synergistic catalytic activity is obtained through nanotube morphology regulation, Cl and S element doping, and heterojunction engineering, laying a solid foundation for the construction of the COP_{SF} system. The nanotube morphology, Cl, S doping of $CN_{Cl/S}$, the nanoflower morphology, S vacancy of MoS_{2v}, and the successful composite of $CN_{Cl/S}$ and MoS_{2v} can be clearly observed through characterizations (Text S4, Figs. S1–4). Interestingly, during XPS analysis (Fig. S3), the peaks of $CN_{Cl/S}$ all undergo a red shift after recombination, while the peaks of MoS_{2v} all undergo a blue shift under lighting conditions. This is related to the inter boundary charge migration effect, which may be caused by the formation of build-in electric field (IEF) during the construction of heterostructures, the Coulombic attraction between charges and the capture of charge carriers by intermediate energy levels [28]. The primary limitations of the individual CO and P_{SF} systems is the low activation efficiency of O_3 and H_2O_2. In the COP_{SF} system, photogenerated e$^-$ can spontaneously promote the production of H_2O_2 and the activation of O_3 and H_2O_2. The combination of two n-type semiconductors of $CN_{Cl/S}$ and MoS_{2v} remarkably intensified the generation of photo-electrons in COP_{SF}. However, the utilization of carriers is also determined by their separation and migration processes to participate in surface redox reactions. Factors such as band structure, IEF, and defect sites (such as Cl, S doping, S vacancy) can significantly affect the carrier migration behaviors. Therefore, exploring the charge carrier transport mechanism influenced by these factors is of great significance for rational materials design to improve e$^-$ utilization and synergistic catalytic activity of COP_{SF}.

The band structure of $CN_{Cl/S}$/MoS_{2v} is obtained through the Kubelka-Munk function of UV–vis conversion, XPS-VB and Mott-Schotty curve (Fig. S5). As shown in Fig. 3c, MoS_{2v} has a more negative CB position (−1.15 eV), while $CN_{Cl/S}$ has a more positive VB position (1.46 eV). According to the positive slope of Mott-Schottky curve, both $CN_{Cl/S}$ and MoS_{2v} are e$^-$ oriented n-type semiconductors. The IEF can be further explored through ultraviolet photo-electron spectroscopy (UPS) characterization. Through Eq. S2, the work functions (WF) of $CN_{Cl/S}$ and MoS_{2v} can be obtained to be 3.68 and 3.94 eV, respectively (Fig. 3a, b). Additionally, DFT simulation results also show that $CN_{Cl/S}$ has greater WF than MoS_{2v} (Fig. S8, S9). Notably, the intrinsic semiconductor of MoS_{2v} has the maximum WF (6.2 eV), but the presence of S vacancy greatly changes the energy band and Fermi level (EF) of MoS_{2v}, providing new channels for carrier transport at the $CN_{Cl/S}$/MoS_{2v} interface. The number of valence electron of O, Cl and S are all greater than N. On the premise of achieving fine adjustment of electronic band structure, the doping of donor element will promote EF of n-type semiconductor shift towards CB[29], resulting in an increase in EF of $CN_{Cl/S}$ and higher than that of MoS_{2v}.

The schematic diagram of energy bands can be obtained as shown in Fig. 3c, S6 and S9. Under the effect of the potential difference at the heterojunction interface, the e$^-$ in $CN_{Cl/S}$ with higher EF will flow to MoS_{2v} until the EF on both sides is flush, thus forming an IEF from CN to MS. Under the influence of IEF, the interface charge distribution is rebalanced, causing the energy bands of $CN_{Cl/S}$ and MoS_{2v} to bend upwards and downwards, respectively. The differential charge distribution of $CN_{Cl/S}$/MoS_{2v} also proves this process (Fig. 3d). The directional charge flow in $CN_{Cl/S}$/MoS_{2v} generates charge depletion and accumulation layers at the interfaces of $CN_{Cl/S}$ and MoS_{2v}, respectively. It will

affect the migration pathway of excited charge carriers and the adsorption effect of O_3 due to its electrophilic properties.

The migration channel of excited carriers in $CN_{Cl/S}$/MoS_{2v}-COP_{SF} system is complex. Under the excitation of photons higher than the band gap energy, the ground state electrons transition to higher levels, forming conduction band (CB) composed of the orbits of the excited state e$^-$ and valence band (VB) composed of the ground state empty orbits. According to the classic Jablonski diagram, excited state e$^-$ cannot completely migration to the surface of $CN_{Cl/S}$/MoS_{2v}, but may be transformed between vibration energy levels or electronic energy levels through vibrational relaxation (VR), fluorescence, internal conversion, intersystem crossing, phosphorescence and so on. Among them, the VR process of excited state e$^-$ guide band edge and defect levels and the radiative recombination process in the form of fluorescence are the common channels of e$^-$ decay [30].

Based on the above analysis, the possible migration channels of photo generated e$^-$ in $CN_{Cl/S}$/MoS_{2v}-COP_{SF} system is shown in Fig. 3e. The radiation recombination (①, ②) of excited state e$^-$ direction ground state is the most common and main decay path. The transmission channels of e$^-$ interactions between $CN_{Cl/S}$ and MoS_{2v} include CB-CB (nonradiative quenching pathway) and CB-VB, and the influencing factors are very complex. Channels ⑤ and ⑥ are hindered by Schottky barrier formed by the upward bending of the CB on the CN side and the Coulomb repulsion force caused by the e$^-$ accumulation layer on MoS_{2v} side. And channel ⑤ is difficult to achieve the transfer from low CB to high CB. Due to the negative correlation between the magnitude of Coulomb force and distance (Eq. S3), the Coulombic gravity that can promote the occurrence of channel ④ is minimized. The resistance to channel ③ is relatively small. However, dynamically, there is repulsive resistance in the e$^-$ migration from CB to CB. Thermodynamically, the e$^-$ migration from high CB to low CB results in a decrease in reduction potential. In summary, the probability of various channel modes occurring varies, but the transmission of e$^-$ interactions can greatly reduce the fluorescence recombination intensity and transmission resistance and improve the carrier utilization efficiency (PL and EIS, Fig. S10 and S11).

The carrier decay duration is obtained by bi-exponential model fitting of time-resolved photoluminescence (TRPL) (Eq. S4, S5) to verify the positive impact of the factors analyzed above on carrier migration (Fig. 3f, Table S7). According to the kinetic analysis of biomolecular trapping model [31], as a non-composite single catalyst, the τ_{avg} value of $CN_{Cl/S}$ is only related to trap-mediated recombination (short amplitude exponential 1) and bimolecular recombination (long amplitude exponential 2), so the smaller τ_{avg} value corresponds to the higher recombination rate of carriers [32]. However, the τ_{avg} value of composite materials shows an opposite trend [33]. As mentioned above, the construction of heterojunctions provides a new channel for non-radiative composite of e$^-$ interactions, resulting in a significant decrease in the τ_{avg} value of $CN_{Cl/S}$/MoS_{2v} (3.88 ns) compared to $CN_{Cl/S}$ (5.43 ns), which is further confirms the positive effect of IEF formation on carrier migration in $CN_{Cl/S}$/MoS_{2v}. Compared to the reported catalytic materials, $CN_{Cl/S}$ and $CN_{Cl/S}$/MoS_{2v} exhibit superior carrier lifetime and transfer efficiency, respectively (Table. S8). Meanwhile, it has been demonstrated that defect sites such as S vacancy may cause the generation of defect energy levels [34]. Comparing the contribution of different components in $CN_{Cl/S}$ and $CN_{Cl/S}$/MoS_{2v} only, it can be found that the proportion of trap mediated recombination in $CN_{Cl/S}$/MoS_{2v} is significantly higher than that in $CN_{Cl/S}$, which further confirming the increase of defect sites in $CN_{Cl/S}$/MoS_{2v}. Furthermore, the capture of carriers by defect sites and the reduction in thickness of 2D materials shorten the distance of carrier transport to the surface to reduce the decay. In summary, the doping of elements and the presence of defect sites alter the WF of $CN_{Cl/S}$ and MoS_{2v} intrinsic structures. During the construction of heterostructure, the difference in EF forms IEF and causes band bending, resulting in Schottky barriers and rectification junctions. Under the influence of the above factors, the excited e$^-$

undergoes inter boundary transmission, leading to significant reduction in the fluorescence radiation recombination of photo-generated carriers, yielding increased e^- for the synergistic catalysis in $CN_{Cl/S}/MoS_{2v}$-COP_{SF}.

In addition to the positive impact of carrier migration on synergistic catalytic activity, Cl, S doping, S vacancies, and IEF derived from heterojunction engineering also can directly promote the catalytic activity of COP_{SF} system. Photogenerated e^- in P_{SF} can directly react with H_2O or dissolved O_2, but the solubility of O_3 in water is lower, and O_3 needs to be first adsorbed near the catalyst before the catalytic reaction can proceed. $CN_{Cl/S}/MoS_{2v}$ shows promoted O_3 adsorption energy (EA-O_3) compared with $CN_{Cl/S}$ (Fig. 4a). The difference in EA-O_3 may be related to the electrophilic and nucleophilic dual characteristics of O_3. The O element from cyanuric acid raw material replaces the edge -NH_2 in $CN_{Cl/S}$ synthesis process to generate -OH. These two functional groups both have e^- withdrawing inductive and e^- donor conjugation effect. Based on the difference of electronegativity, -NH_2 has stronger e^- donor ability [35], so the presence of -OH slightly reduces EA-O_3. The Cl element is also doped in the form of replacing -NH_2, but compared to N, the orbital of non-periodic Cl overlaps less with the orbital of C, so -Cl exhibits stronger e^- withdrawing inductive effect. The decrease in electrostatic potential at -Cl also confirms this conclusion (Fig. S12). Furthermore, on the basis of localized bonds, the enhanced polarity of -Cl compared to -NH_2 is more conducive to the adsorption of polar molecule O_3 [36]. Although the doping of S element cannot offset the negative effects of -OH substitution, it is also beneficial for the adsorption of O_3. The dual effects of Cl and S reduce EA-O_3 significantly. Additionally, when the S vacancy exists, the originally limited charge at S atom tends to flow to the surrounding of Mo atoms, improving the delocalized electron density near Mo [37]. For example, S vacancy is shown as a high potential in the electrostatic potential diagram (Fig. S13), which significantly improves the adsorption affinity of O_3. The charge separation caused by IEF influence the kinetic process of O_3. According to the calculation of EA-O_3, O_3 is more easily attracted by the charge accumulation layer on the MoS_{2v} side. The differential charge of $CN_{Cl/S}/MoS_{2v}$ in O_3 adsorption state is shown in Fig. 4b and c. O_3 is greatly influenced by S vacancy and IEF. It can be adsorbed on the surface of $CN_{Cl/S}/MoS_{2v}$, causing charge flow from $CN_{Cl/S}/MoS_{2v}$ towards O_3 and changing the bond length and angle of O_3 molecules (Fig. S15a, b), resulting in a fracture trend of the edge O bonds. The adsorbed O (*O) has can be an important intermediate state for the generation of other ROS in both CO and P_{SF} processes [17], and may act as a synergistic species in $CN_{Cl/S}/MoS_{2v}$-COP_{SF} system.

3.3. Mechanism of reactive species transformation and synergistic reaction activity in $CN_{Cl/S}/MoS_{2v}$-COP_{SF} system

The enhancement of carrier migration and O_3 adsorption capacity creates a favorable synergistic reaction environment for COP_{SF} system. In addition to active species such as e^- and ROS, the reaction characteristics of target pollutants also affect the active species transfer within the system. Moreover, the synergistic reaction activity of COP_{SF} system can be reflected to some extent by comparing the differences in PNP degradation pathways within $CN_{Cl/S}/MoS_{2v}$-P_{SF}, $CN_{Cl/S}/MoS_{2v}$-CO and $CN_{Cl/S}/MoS_{2v}$-COP_{SF} systems.
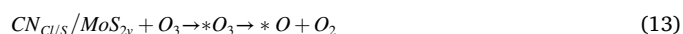
In the range of pH= 4–9, PNP exists in two forms: molecular state (PNP1) and ionic state (PNP2). The main active sites of both forms of PNP are N7 and -NO_2 group. However, their surface electrostatic potential and the electrophilic/nucleophilic properties can be different. Fig. 5a shows that PNP1 has a more uniform electrostatic potential distribution, and its active sites are mainly O9 and N7 with both electrophilic and nucleophilic properties. N8 is susceptible to electrophilic attacks due to the influence of unsaturated bonds, and O10, C1, C3 are more susceptible to nucleophilic attacks (electrophilic properties). The ionic form of PNP2 significantly enhances the electrophilic and nucleophilic properties of O7, while O9, O10, C3, C1 and C5 all exhibit strong
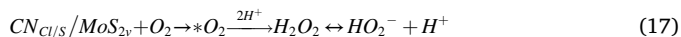
reactivity toward ROS.

The difference of active sites in the above reactions provides a variety of possible pathways for PNP degradation, and the differences among $CN_{Cl/S}/MoS_{2v}$-P_{SF}, $CN_{Cl/S}/MoS_{2v}$-CO and $CN_{Cl/S}/MoS_{2v}$-COP_{SF} systems can be visually observed through LCMS (Fig. S18-S21). In the widely recognized mechanism of pollutant degradation, P_{SF} system mainly decomposes pollutants gradually through h^+, $^\bullet$OH, $O_2^{\bullet-}$ and ROS generated by H_2O_2 activation [38,39]. In contrast, CO system may also generate various epoxide and carbonyl compounds through electrophilic, nucleophilic and Criegee reactions [40]. Therefore, because of the limited reaction active sites and thus insufficient ROS, the degradation efficiency of P_{SF} system is lower than CO and COP_{SF} systems. CO system has two pathways: O_3 direct and indirect reaction. Pollutants are often first oxidized into polymer compounds with high molecular weight, and then further degraded through ROS [41]. The degradation pathway of PNP in COP_{SF} system is different from that in both P_{SF} and CO systems. The intermediate products include various ring opening and substitution products in P_{SF} system, as well as dimeric compounds that are easily produced in CO system. Comfortingly, no refractory macromolecular epoxy polymers of CO system are detected in COP_{SF} system. This may be related to the synergistic reaction of active species in the system that promoted the activation of O_3 and H_2O_2, and reducing the direct reaction of O_3.

The production and transfer of *O and H_2O_2 from CO and P_{SF} accordingly are important intermediates to coordinate synergistic reactions in the COP_{SF} system. *O can further react with H^+, OH^-, O_3, to produce ROS such as $^\bullet$OH and $O_2^{\bullet-}$ [42], and catalyze the formation of HO_2^- (Eqs. 14–16). As a control step in CO process (Fig. 2a), HO_2^- can participate in the ROS chain reactions at an extremely fast reaction rate [12]. The synergistic reaction mechanism is further inferred through the detection of active species. It can be observed form Fig. 5b, c that the response intensity e^- and $^\bullet$OH in $CN_{Cl/S}/MoS_{2v}$-COP_{SF} system are significantly enhanced compared to the $CN_{Cl/S}/MoS_{2v}$-CO and $CN_{Cl/S}/MoS_{2v}$-P_{SF} systems. DFT simulation calculations is used to further infer the transfer path of active components within $CN_{Cl/S}/MoS_{2v}$-COP_{SF} system (Fig. 5d, S22). As analyzed about EA-O_3 (Fig. 4a), O_3 dispersed around the $CN_{Cl/S}/MoS_{2v}$ is easily adsorbed by on the side of MoS_{2v} to form *O_3. The delocalized e^- in Π_3^4 bond of O_3 tends to migrate in the direction of reducing the activation energy of the reaction [43]. The edge O atom is easy to be attracted, showing a trend of being far away from center O atom until the chemical bond breaks and generates *O (Eq. 14). Furthermore, The O_2 surrounding $CN_{Cl/S}/MoS_{2v}$ also spontaneously generates *O_2, which can directly react with H^+ or further decompose to generate *O to generate H_2O_2 (Eqs. 12, 17).

Possible synergistic pathways of active species through quenching experiments and the above analysis is inferred. From Fig. 5e and S24, $CN_{Cl/S}/MoS_{2v}$-COP_{SF} system is least constrained by a single active component due to multiple reaction pathways compared to the other two systems (avg=0.476). $^\bullet$OH is more likely to react directly with PNP due to its high oxidation reduction potential. Based on the variety of active species, the role of $^\bullet$OH is not irreplaceable. $O_2^{\bullet-}$ has the greatest impact on $CN_{Cl/S}/MoS_{2v}$-COP_{SF} system, and the charge carriers transferred to the surface can react with O_2 and O_3 in one or more steps to generate $O_2^{\bullet-}$. And $O_2^{\bullet-}$ is likely to act as an intermediate to synergize the active components in COP_{SF} system [44].

$$CN_{Cl/S}/MoS_{2v} + hv \rightarrow e^- + h^+ \tag{9}$$

$$e^- + O_2 \rightarrow O_2^{\bullet-} \tag{10}$$

$$e^- + O_3 \rightarrow O_3^{\bullet-} \xrightarrow{H^+} \bullet OH + O_2 \tag{11}$$

$$*O_2 \rightarrow *O + \bullet O \tag{12}$$

$$CN_{Cl/S}/MoS_{2v} + O_3 \rightarrow *O_3 \rightarrow *O + O_2 \tag{13}$$

$$*O + H^+ \rightarrow *OH \rightarrow \bullet OH \tag{14}$$

$$*O + OH^- \rightarrow *OOH^- \rightarrow HO_2^- \rightarrow HO_2\bullet \tag{15}$$

$$*O + O_3 \rightarrow *OO + O_2 \rightarrow O_2^{\bullet-} + O_2 \tag{16}$$

$$CN_{Cl/S}/MoS_{2v} + O_2 \rightarrow *O_2 \xrightarrow{2H^+} H_2O_2 \leftrightarrow HO_2^- + H^+ \tag{17}$$

$$O_3 + HO_2^- \rightarrow \bullet OH + O_2^{\bullet-} + O_2 \tag{18}$$

In conclusion, the main active species transfer and synergistic reaction in $CN_{Cl/S}/MoS_{2v}$-COP_{SF} system is summarized as Eqs. 9–18 and Fig. 5f. The presence of IEF causes the formation of e^- accumulation layer on the side of MoS_{2v} and promote the migration of charge carriers, resulting more photo-generated e^- and O_3 converge on the surface of $CN_{Cl/S}/MoS_{2v}$ to participate in synergistic reaction (Eqs. 9–11). As an important synergistic active species, *O can be produced by *O_2 and *O_3 (Eqs. 12, 13), and reacts with H^+, OH^-, O_3. to produce H_2O_2, HO_2^- and other ROS (Eqs. 14–16)·H_2O_2 and HO_2^- not only react with O_3 to produce ROS (Eqs. 17, 18), but also has a much longer lifespan than free radical species [15]. Thus, the generation of these reactive oxygen intermediates is beneficial to prolong the transfer distance, improve reaction activity, and improve the utilization efficiency of ROS. Due to the synergistic effect within $CN_{Cl/S}/MoS_{2v}$-COP_{SF}, the production of refractory epoxide polymers decreases and the generation of active species increases.

3.4. Correlation of descriptors and local/global properties in synergistic catalysis and reaction process of $CN_{Cl/S}/MoS_{2v}$-COP_{SF} system

Pearson correlation coefficient is used to calculate the correlation of common descriptors in DFT simulation and environmental catalysis in $CN_{Cl/S}/MoS_{2v}$-P_{SF}, $CN_{Cl/S}/MoS_{2v}$-CO and $CN_{Cl/S}/MoS_{2v}$-COP_{SF} systems (Table S10). In addition to the descriptors mentioned earlier, the descriptors used in this work also include molecule total energy (TE), EHOMO, ELUMO, specific surface activity (ASS), condensed dual descriptor (CDD, Eq. S6-S8), chemical potential (μ, numerically equal to electronegativity), hardness (η, which is related to the difficulty of electron cloud strain) and global electrophilicity index (GEI). The results are shown in Fig. 6a, S25. As shown in the first row/column, k doesn't show significant correlation with single descriptor. The correlation between condensed Fukui function descriptors (fn, fe and $f0$) and k is stronger compared to other descriptors. Excluding errors caused by algorithms, these favorable descriptors may be due to their true reflection of molecular electrophilic and nucleophilic properties that determine the oxidation kinetics with ROS [45,46]. This characteristic is mostly used to predict the active reaction sites of target pollutants. The higher the absolute value, the more susceptible it is to electrophilic, nucleophilic, or free radical attacks [18,47]. This may be reflected on the catalyst because the higher the activity, the easier it is to attract the aggregation of active components and participate in the degradation of target pollutants. The band structure (VB, CB, BG) of catalytic materials shows strong correlation with other descriptors. While this phenomenon is not reflected in WF, which has a significant impact on charge carriers.
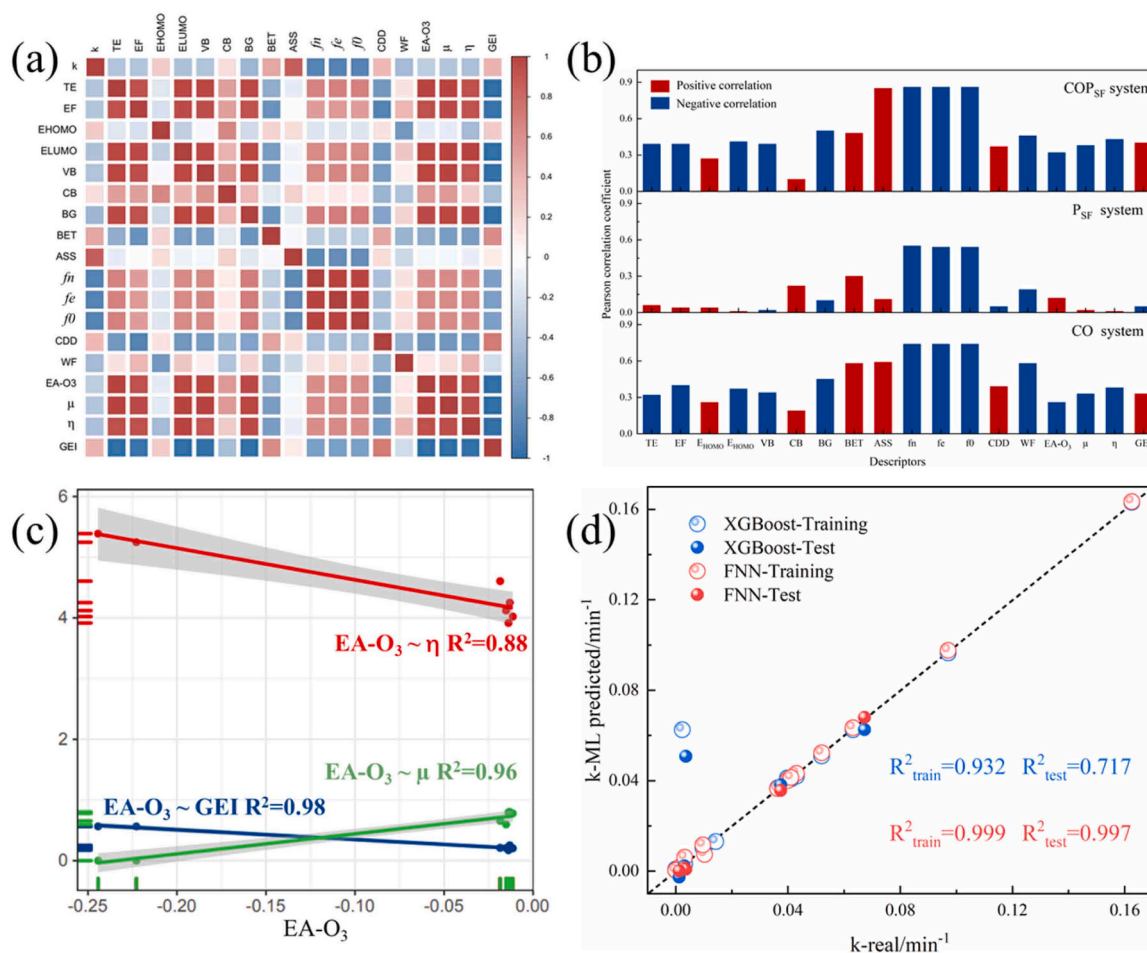

Fig. 6. (a) Pearson correlation coefficient heatmap of different descriptors in COP_{SF} system. (b) The correlation coefficients between each descriptor and k in different systems obtained from the heatmap of P_{SF}, CO and COP_{SF} systems (blue: negative correlation, red: positive correlation). (c) Linear regression fitting diagram of the correlation between EA-O_3 and GEI, μ and η. (d) Plots of the measured k (k-real) vs predicted k (k-ML predicted) for XGBoost and FNN models.

Comparing the correlation trend of descriptors in different systems with respect to k (Fig. 6b), although some descriptors show opposite correlation in P_{SF} and CO systems, the correlation trend of band structure (VB, CB, BG), BET, condensed Fukui function descriptors (fn, fe and f0), WF, etc. with strong correlation with k are consistent. This is also an important reason why the COP_{SF} system can achieve efficient synergism in addition to the influence of active species reaction chain.

There is strong correlation between $EA-O_3$ and η, μ and GEI (−0.94, 0.98, and −0.99, respectively). Lewis acid has been widely recognized as active site for O_3 adsorption and activation [48]. As an important quantitative evaluation indicator for Lewis acid, GEI has significant impacts on O_3 adsorption and activity [49]. From the definition formula of GEI (Eq. S9-S11), the stronger the electronegativity (the greater the μ), the easier the electron cloud is to deform (the smaller the η), the easier it is to accept e^-. The linear regression diagram (Fig. 6c) shows that the more easily the electron cloud deforms, the stronger the electronegativity and the higher the e^- affinity, the higher the adsorption activity of O_3.

In multi-component synergistic systems, the influencing factors of reaction activity are complex and diverse. A large number of synergistic factors have caused difficulties in the experimental verification process. Using ML to establish descriptor–activity relationship can greatly reduce the workload and is of great significance to the design and improvement of new systems. Using common ML models: FNN, NB, RT, RF and XGBoost, the descriptors-k in Fig. 6a are randomly divided into training and testing sets for prediction (Fig. 6d, S26). As a typical generative model, NB uses joint probabilities of independent datasets for prediction [50], which is not suitable for predicting multi-component correlation systems in this work. Although tree regression algorithms (RT, RF) perform well in the training process, they are affected by the small size of the dataset and the extreme values caused by $MoS_{2v}-P_{SF}$, $CN_{Cl/S}/MoS_{2v}-COP_{SF}$, resulting in significant deviations in the predicted results. XGBoost model shows better prediction results than the models mentioned above (R^2_{train}=0.932, R^2_{test}=0.717). Although it can use the second Taylor series to calculate the Loss function and adjust parameters to avoid over fitting, and has a more suitable application than other models in catalytic ozonation [17,51], it is still affected by the extreme values in data set. After normalizing the dataset, the FNN model (with ReLU as the hidden layer and sigmoid as the output layer to reduce loss) performed the best in prediction. As a type of Artificial Neural Network (ANN), FNN can effectively predict and model nonlinear and highly complex datasets, which has significant advantages in prediction accuracy, stability, and other aspects[52,53], and has gradually been developed and applied in the environmental field [54]. The FNN model exhibits the highest R2 (R^2_{train}=0.999, R^2_{test}=0.997), indicating that compared to other selected models, FNN is the most suitable for the dataset of this system.

3.5. Petrochemical wastewater treatment

The effectiveness of the $CN_{Cl/S}/MoS_{2v}-COP_{SF}$ system in treating petrochemical wastewater is analyzed through excitation-emission matrix (EEM) fluorescence. The dissolved organic matters (DOM) in petrochemical wastewater are divided into five regions (Fig. S27, S28)
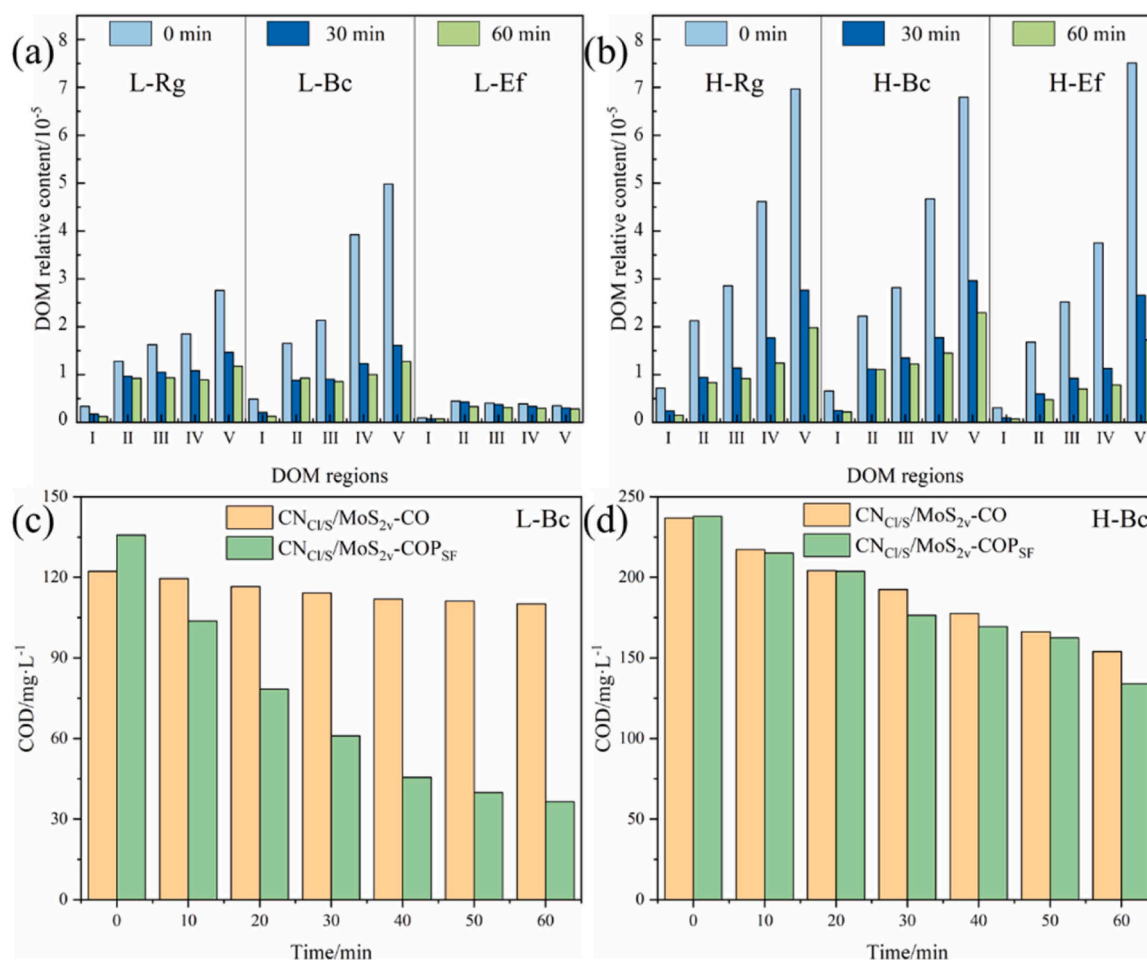

Fig. 7. Data visualization DOM degradation effect diagram obtained by integration of EEM fluorescence: (a) LPW: wastewater of regulating tank (L-Rg), biochemical tank (L-Bc) and effluent tank (L-Ef), (b) HPW: wastewater of regulating tank (H-Rg), biochemical tank (H-Bc) and effluent tank (H-Ef). Comparison of COD degradation map in $CN_{Cl/S}/MoS_{2v}-CO$ and $CN_{Cl/S}/MoS_{2v}-COP_{SF}$ systems for (c) H-Bc and (d) L-Bc.

[55]. Region I-V is tyrosine-like, tryptophan-like, fulvic-like acids, soluble microbial products and humic-like acids, respectively. The strongest fluorescent responder in LPW is aromatic protein, which is believed to be related to human chemical industry in existing environmental studies. From Fig. 7a, S27, the original processing process can effectively treat LPW, while $CN_{Cl/S}/MoS_{2v}$-COP_{SF} system can further remove DOM on this basis. In addition, the treatment effect of $CN_{Cl/S}/MoS_{2v}$-CO system on L-Bc is limited. As mentioned earlier, the CO process may generate epoxy compounds, and the production of free radicals is relatively low. The COD of L-Bc can be reduced to below 50 mg/L after 60 min by $CN_{Cl/S}/MoS_{2v}$-COP_{SF} system, which greatly shortens the reaction time compared to the time-consuming biological treatment process in the original process (Fig. 7c). The composition of HPW is relatively complex, with the main fluorescence peaks distributed in the II-V four regions. The original treatment process did not significantly remove DOM from it (Figs. S28, 7b). The $CN_{Cl/S}/MoS_{2v}$-COP_{SF} system exhibits significantly enhanced treatment efficiency for HPW compared to original treatment process and $CN_{Cl/S}/MoS_{2v}$-CO system (Fig. 7b, d, S29). According to Fig. S31, the $CN_{Cl/S}/MoS_{2v}$-COP_{SF} system exhibits enhanced reaction activity in alkaline water, and HPW alkaline water is beneficial for enhancing system activity. Notably, the Cl^- content in H-Rg is greater than 1000 mg/L, and H-Ef still contains a high Cl^- content (Table S1). Cl^- has dual promoting and inhibiting effects in the $CN_{Cl/S}/MoS_{2v}$-COP_{SF} system, and the mechanism of is complex. The promoting effect may be due to the chlorine based reactive species, such as ClO and $ClOH^{\bullet-}$ and $\cdot Cl/Cl_2^{\bullet-}$ radicals, which screened the ROS and may directly react with the pollutants to form chlorinated byproducts. Additionally, the presence of massive Cl will promote gas-liquid and liquid internal mass transfer in O_3-$CN_{Cl/S}/MoS_{2v}$-wastewater three-phase system [56]. The inhibiting effect including (1) the prohibited pollutant of the adsorption and occupation of catalytic sites, (2) the ineffective consumption of O_3 by Cl^-, and (3) the disruption of the ROS reaction chain in COP_{SF} system through the consumption of more oxidizing $^{\bullet}OH$ (compared with chlorine species). Spcifically, Cl^- can participate in the free radical reaction chain, generate chlorine free radical ($^{\bullet}Cl$, 2.4 eV), dichloroanionic free radical ($^{\bullet}Cl_2^-$, 2.0 eV) and other pollutants to participate in the degradation, and can also react with $^{\bullet}OH$ and consume active components [57]. Moreover, single factor simulation experiment (Fig. S32) shows that the difference in concentration between pollutants and Cl^- can also affect its effectiveness. When the Cl^- content is significantly higher than PNP, Cl^- exhibits a promoting effect on PNP degradation. This also conforms to the water quality situation of HPW (Table S1). Overall, the synergistic catalysis and reaction activity of $CN_{Cl/S}/MoS_{2v}$-COP_{SF} system endows it with excellent treating performance for complex petrochemical wastewater. And the $CN_{Cl/S}/MoS_{2v}$-COP_{SF} system exhibits enhanced LPW and HPW treatment effects compared to the original treatment process.

4. Conclusion

Catalytic ozonation synergistic photo-self-Fenton (COP_{SF}) system was first constructed based on the development of Cl, S doped carbon nitride nanotube composite molybdenum disulfide with S vacancy ($CN_{Cl/S}/MoS_{2v}$) to improve the treatment efficiency of refractory pollutants in petrochemical industry. The enhanced removal activity of refractory pollutants ($k = 0.18$ min^{-1}), the synergistic generation and decomposition process of H_2O_2 (k_g=0.014 mg•(L•min)$^{-1}$, k_d= 0.062 min^{-1}), and the synergistic effect of CO and P_{SF} (synergistic factor=1.35) in $CN_{Cl/S}/MoS_{2v}$-COP_{SF} system have been proven. The detailed charge carries migration channels under and the synergistic catalytic activity of carriers for catalytic O_3 and self-produced H_2O_2, and the enhanced reactive activity of reactive species were explored. Descriptors with strong correlation with k have similar correlation trends within the CO, P_{SF} and COP_{SF} system, which is an important reason for efficient synergism. And FNN model has the highest prediction accuracy of $CN_{Cl/S}/MoS_{2v}$-COP_{SF} system. For the six types of actual petrochemical

wastewater with low salinity-low COD low and high salinity-high COD, $CN_{Cl/S}/MoS_{2v}$-COP_{SF} system all showed better treatment effects than the original treatment process. This study provides reference for the treatment of petrochemical wastewater, in-depth research on synergistic mechanisms, and treatment of a large number of complex factors.

CRediT authorship contribution statement

Benjie Zhu: Conceptualization; Methodology; Software; Formal analysis; Investigation; Writing – original draft; Writing – review & editing. **Yuting Wang:** Investigation; Validation. **Chenxing Li:** Validation. **Fei Gao:** Validation. **Fang Liu:** Resources; Writing – review & editing; Supervision; Project administration; Funding acquisition. **Guofei Jiang:** Investigation. **Huaqing Zhang:** Software; Data curation. **Xiaoguang Duan:** Supervision; Writing – review & editing.

Declaration of Competing Interest

The authors declare that they have no known competing financial interests or personal relationships that could have appeared to influence the work reported in this paper.

Data availability

No data was used for the research described in the article.

Acknowledgments

Appendix A. Supporting information

Supplementary data associated with this article can be found in the online version at doi:10.1016/j.apcatb.2023.123408.

References

[1] D. Sun, S. Shao, Y. Zhang, Q. Yang, H. Hou, X. Quan, Integrated analysis of the water-energy-environmental pollutant nexus in the petrochemical industry, Environ. Sci. Technol. 54 (2020) 14830–14842.

[2] M. Kalantari, S.S. Moghaddam, F. Vafaei, Global research trends in petrochemical wastewater treatment from 2000 to 2021, Environ. Sci. Pollut. Res. Int. 30 (2023) 9369–9388.

[3] A.I. Adetunji, A.O. Olaniran, Treatment of industrial oily wastewater by advanced technologies: a review, Appl. Water Sci. 11 (2021).

[4] N. Morin-Crini, E. Lichtfouse, G. Liu, V. Balaram, A.R.L. Ribeiro, Z. Lu, F. Stock, E. Carmona, M.R. Teixeira, L.A. Picos-Corrales, J.C. Moreno-Piraján, L. Giraldo, C. Li, A. Pandey, D. Hocquet, G. Torri, G. Crini, Worldwide cases of water pollution by emerging contaminants: a review, Environ. Chem. Lett. 20 (2022) 2311–2338.

[5] C.V.T. Rigueto, M.T. Nazari, L.Á. Massuda, B.E.P. Ostwald, J.S. Piccin, A. Dettmer, Production and environmental applications of gelatin-based composite adsorbents for contaminants removal: a review, Environ. Chem. Lett. 19 (2021) 2465–2486.

[6] K. Wang, X. Chen, D. Yan, Z. Xu, P. Hu, H. Li, Petrochemical and municipal wastewater treatment plants activated sludge each own distinct core bacteria driven by their specific incoming wastewater, Sci. Total Environ. 826 (2022), 153962.

[7] M. Priyadarshini, I. Das, M.M. Ghangrekar, L. Blaney, Advanced oxidation processes: performance, advantages, and scale-up of emerging technologies, J. Environ. Manag. 316 (2022) 115295.

[8] S. Zhan, H. Huang, C. He, Y. Xiong, P. Li, S. Tian, Controllable synthesis of substitutional and interstitial nitrogen-doped ceria: the effects of doping sites on enhanced catalytic ozonation of organic pollutants, Appl. Catal. B: Environ. 321 (2023).

[9] J. Cui, L. Li, S. Shao, J. Gao, K. Wang, Z. Yang, S. Zeng, C. Diao, Y. Zhao, C. Hu, Regulating the metal–support interaction: double jump to reach the efficiency apex of the Fe–N4-catalyzed fenton-like reaction, ACS Catal. 12 (2022) 14954–14963.

[10] Y. Zhang, X. Zhang, S. Wang, Recent advances in the removal of emerging contaminants from water by novel molecularly imprinted materials in advanced oxidation processes-A review, Sci. Total Environ. 883 (2023), 163702.

[11] B. Zhu, G. Jiang, S. Chen, F. Liu, Y. Wang, C. Zhao, Multifunctional Cl-S double-doped carbon nitride nanotube unit in catalytic ozone oxidation synergistic

photocatalytic system: generation of ROS-rich region and effective treatment of organic wastewater, Chem. Eng. J. 430 (2022).

[12] R.R. Solís, S. Medina, O. Gimeno, F.J. Beltrán, Solar photolytic ozonation for the removal of recalcitrant herbicides in river water, Sep. Purif. Technol. 212 (2019) 280–288.

[13] A. Gopakumar, P. Ren, J. Chen, B.V. Manzolli Rodrigues, H.Y. Vincent Ching, A. Jaworski, S.V. Doorslaer, A. Rokicinska, P. Kustrowski, G. Barcaro, S. Monti, A. Slabon, S. Das, Lignin-supported heterogeneous photocatalyst for the direct generation of H(2)O(2) from seawater, J. Am. Chem. Soc. 144 (2022) 2603–2613.

[14] J. Gu, J. Xie, S. Li, G. Song, M. Zhou, Highly efficient electro-peroxone enhanced by oxygen-doped carbon nanotubes with triple role of in-situ H2O2 generation, activation and catalytic ozonation, Chem. Eng. J. 452 (2023).

[15] X. Liu, X. Yan, W. Liu, Q. Yan, M. Xing, Switching of radical and nonradical pathways through the surface defects of Fe(3)O(4)/MoO(x)S(y) in a Fenton-like reaction, Sci. Bull. (Beijing) 68 (2023) 603–612.

[16] W.J. Ong, L.L. Tan, Y.H. Ng, S.T. Yong, S.P. Chai, Graphitic carbon nitride (g-C3N4)-based photocatalysts for artificial photosynthesis and environmental remediation: are we a step closer to achieving sustainability? Chem. Rev. 116 (2016) 7159–7329.

[17] G. Yu, Y. Wu, H. Cao, Q. Ge, Q. Dai, S. Sun, Y. Xie, Insights into the mechanism of ozone activation and singlet oxygen generation on n-doped defective nanocarbons: a DFT and machine learning study, Environ. Sci. Technol. 56 (2022) 7853–7863.

[18] H. Ji, P. Du, D. Zhao, S. Li, F. Sun, E.C. Duin, W. Liu, 2D/1D graphitic carbon nitride/titanate nanotubes heterostructure for efficient photocatalysis of sulfamethazine under solar light: catalytic "hot spots" at the rutile–anatase–titanate interfaces, Appl. Catal. B: Environ. 263 (2020).

[19] S. Wu, H. Yu, S. Chen, X. Quan, Enhanced photocatalytic H2O2 production over carbon nitride by doping and defect engineering, ACS Catal. 10 (2020) 14380–14389.

[20] J. Peto, T. Ollar, P. Vancso, Z.I. Popov, G.Z. Magda, G. Dobrik, C. Hwang, P. B. Sorokin, L. Tapaszto, Spontaneous doping of the basal plane of MoS(2) single layers through oxygen substitution under ambient conditions, Nat. Chem. 10 (2018) 1246–1251.

[21] B.C. Zhu, B. Cheng, J.J. Fan, W.K. Ho, J.G. Yu, g-C3N4-based 2D/2D composite heterojunction photocatalyst, Small Struct. 2 (2021).

[22] P. Xia, S. Cao, B. Zhu, M. Liu, M. Shi, J. Yu, Y. Zhang, Designing a 0D/2D S-scheme heterojunction over polymeric carbon nitride for visible-light photocatalytic inactivation of bacteria, Angew. Chem. Int Ed. Engl. 59 (2020) 5218–5225.

[23] N. Luo, C. Chen, D. Yang, W. Hu, F. Dong, S defect-rich ultrathin 2D MoS2: The role of S point-defects and S stripping-defects in the removal of Cr(VI) via synergistic adsorption and photocatalysis, Appl. Catal. B: Environ. 299 (2021).

[24] Y. Yao, Y. Xie, B. Zhao, L. Zhou, Y. Shi, Y. Wang, Y. Sheng, H. Zhao, J. Sun, H. Cao, N-dependent ozonation efficiency over nitrogen-containing heterocyclic contaminants: a combined density functional theory study on reaction kinetics and degradation pathways, Chem. Eng. J. 382 (2020).

[25] L. Gu, X.W. Zhang, L.C. Lei, Degradation of aqueous p-nitrophenol by ozonation integrated with activated carbon, Ind. Eng. Chem. Res 47 (2008) 6809–6815.

[26] D. Yu, F. Wu, J. He, L. Bai, Y. Zheng, Z. Wang, J. Zhang, Tuned layered double hydroxide-based catalysts inducing singlet oxygen evolution: Reactive oxygen species evolution mechanism exploration, norfloxacin degradation and catalysts screen based on machine learning, Appl. Catal. B: Environ. 320 (2023).

[27] T.C.D. Andrew, W. Vermilyea, Bettina M. Voelker, Use of $H_2^{18}O_2$ to measure absolute rates of dark H2O2 production in freshwater systems, Environ. Sci. Technol. 44 (2010) 3066–3072.

[28] C. Cui, X. Zhao, X. Su, N. Xi, X. Wang, X. Yu, X.L. Zhang, H. Liu, Y. Sang, Porphyrin-based donor–acceptor covalent organic polymer/ZnIn2S4 Z-scheme heterostructure for efficient photocatalytic hydrogen evolution, Adv. Funct. Mater. 32 (2022).

[29] K.H. Ye, H. Li, D. Huang, S. Xiao, W. Qiu, M. Li, Y. Hu, W. Mai, H. Ji, S. Yang, Enhancing photoelectrochemical water splitting by combining work function tuning and heterojunction engineering, Nat. Commun. 10 (2019) 3687.

[30] L. Zhang, J. Zhang, H. Yu, J. Yu, Emerging S-scheme photocatalyst, Adv. Mater. 34 (2022), e2107668.

[31] E.V. Pean, S. Dimitrov, C.S. De Castro, M.L. Davies, Interpreting time-resolved photoluminescence of perovskite materials, Phys. Chem. Chem. Phys. 22 (2020) 28345–28358.

[32] Y. Zhang, C. Pan, G. Bian, J. Xu, Y. Dong, Y. Zhang, Y. Lou, W. Liu, Y. Zhu, H2O2 generation from O2 and H2O on a near-infrared absorbing porphyrin supramolecular photocatalyst, Nat. Energy 8 (2023) 361–371.

[33] Z. Liang, Y. Xue, X. Wang, X. Zhang, J. Tian, Structure engineering of 1T/2H multiphase MoS2 via oxygen incorporation over 2D layered porous g-C3N4 for remarkably enhanced photocatalytic hydrogen evolution, Mater. Today Nano 18 (2022).

[34] Y. Peng, M. Geng, J. Yu, Y. Zhang, F. Tian, Yn Guo, D. Zhang, X. Yang, Z. Li, Z. Li, S. Zhang, Vacancy-induced 2H@1T MoS2 phase-incorporation on ZnIn2S4 for boosting photocatalytic hydrogen evolution, Appl. Catal. B: Environ. 298 (2021).

[35] N. Meng, W. Zhou, Y. Yu, Y. Liu, B. Zhang, Superficial hydroxyl and amino groups synergistically active polymeric carbon nitride for CO2 electroreduction, ACS Catal. 9 (2019) 10983–10989.

[36] E. Jennings, A. Kremser, L. Han, T. Reemtsma, O.J. Lechtenfeld, Discovery of polar ozonation byproducts via direct injection of effluent organic matter with online LC-FT-ICR-MS, Environ. Sci. Technol. 56 (2022) 1894–1904.

[37] X. Wang, Y. Zhang, H. Si, Q. Zhang, J. Wu, L. Gao, X. Wei, Y. Sun, Q. Liao, Z. Zhang, K. Ammarah, L. Gu, Z. Kang, Y. Zhang, Single-atom vacancy defect to trigger high-efficiency hydrogen evolution of MoS(2), J. Am. Chem. Soc. 142 (2020) 4298–4308.

[38] X. Zhang, J. Wang, B. Xiao, Y. Pu, Y. Yang, J. Geng, D. Wang, X. Chen, Y. Wei, K. Xiong, Y. Zhu, Resin-based photo-self-Fenton system with intensive mineralization by the synergistic effect of holes and hydroxyl radicals, Appl. Catal. B: Environ. 315 (2022).

[39] Z. Yang, L. Li, J. Gao, S. Zeng, J. Cui, S. Shao, K. Wang, D. Ma, C. Hu, Y. Zhao, Optimizing the band structure of crystalline potassium poly(heptazine imide) for enhanced photocatalytic H2O2 production and pollutant degradation, ACS EST Eng. 2 (2022) 2142–2149.

[40] Y. Wang, X. Duan, Y. Xie, H. Sun, S. Wang, Nanocarbon-based catalytic ozonation for aqueous oxidation: engineering defects for active sites and tunable reaction pathways, ACS Catal. 10 (2020) 13383–13414.

[41] S. Kharel, M. Stapf, U. Miehe, M. Ekblad, M. Cimbritz, P. Falås, J. Nilsson, R. Sehlén, J. Bregendahl, K. Bester, Removal of pharmaceutical metabolites in wastewater ozonation including their fate in different post-treatments, Sci. Total Environ. 759 (2021).

[42] Z. Song, Z. Wang, J. Ma, J. Sun, C. Li, X. Xu, C. Chen, Z. Chen, B. Xu, Y. Jiang, J. Kumirska, E.M. Siedlecka, A. Ikhlaq, F. Qi, O. Ismailova, Molecular levels unveil the membrane fouling mitigation mechanism of a superpotent N-rGO catalytic ozonation membrane: Interfacial catalytic reaction pathway and induced EfOM transformation reactions, Appl. Catal. B: Environ. 319 (2022).

[43] Z.W. Huang, J.X. Liang, D.M. Tang, Y.X. Chen, W.Y. Qu, X.L. Hu, J.X. Chen, Y. Y. Dong, D.R. Xu, D. Golberg, J. Li, X.F. Tang, Interplay between remote single-atom active sites triggers speedy catalytic oxidation, Chem 8 (2022) 3008–3017.

[44] B. Zhu, S. Chen, C. Li, G. Jiang, F. Liu, R. Zhao, C. Liu, Non-metallic hollow porous sphere loaded CN/catalytic ozonation synergistic photocatalytic system: Enhanced treatment of emerging pollutants by three-stage cyclic reaction mechanism, Appl. Catal. B: Environ. 318 (2022).

[45] G. Yu, Y. Xie, Q. Ge, Q. Dai, J. Xu, H. Cao, Mechanism of ozone adsorption and activation on B-, N-, P-, and Si-doped graphene: A DFT study, Chem. Eng. J. 430 (2022).

[46] B. Wang, B. Rong, P.K. Chattaraj, S. Liu, A comparative study to predict regioselectivity, electrophilicity and nucleophilicity with Fukui function and Hirshfeld charge, Theor. Chem. Acc. 138 (2019).

[47] J. Guo, H. Sun, X. Yuan, L. Jiang, Z. Wu, H. Yu, N. Tang, M. Yu, M. Yan, J. Liang, Photocatalytic degradation of persistent organic pollutants by Co-Cl bond reinforced CoAl-LDH/Bi(12)O(17)Cl(2) photocatalyst: mechanism and application prospect evaluation, Water Res. 219 (2022), 118558.

[48] Z. Guo, J. Wei, Z. Wu, Y. Guo, Y. Song, Stabilized N coordinated Cu site in catalytic ozonation: the efficient generation of OH induced by surface hydroxyl groups based on the Lewis acid site, Sep. Purif. Technol. 304 (2023).

[49] A.R. Jupp, T.C. Johnstone, D.W. Stephan, The global electrophilicity index as a metric for Lewis acidity, Dalton Trans. 47 (2018) 7029.

[50] G. Carvajal, D.J. Roser, S.A. Sisson, A. Keegan, S.J. Khan, Modelling pathogen log10 reduction values achieved by activated sludge treatment using naive and semi naive Bayes network models, Water Res 85 (2015) 304–315.

[51] T. Chen, C. Guestrin, XGBoost, Proceedings of the 22nd ACM SIGKDD International Conference on Knowledge Discovery and Data Mining, 2016, pp. 785–794.

[52] A. Azad, H. Karami, S. Farzin, S.-F. Mousavi, O. Kisi, Modeling river water quality parameters using modified adaptive neuro fuzzy inference system, Water Sci. Eng. 12 (2019) 45–54.

[53] M. Li, L. Fu, L. Deng, Y. Hu, Y. Yuan, C. Wu, A tailored and rapid approach for ozonation catalyst design, Environ. Sci. Ecotechnol 15 (2023), 100244.

[54] X. Wang, X. Tian, Z. Liao, Framework for hyperparameter impact analysis and selection for water resources feedforward neural network, Water Resour. Manag. 36 (2022) 4201–4217.

[55] D. Cha, S. Park, M.S. Kim, T. Kim, S.W. Hong, K.H. Cho, C. Lee, Prediction of oxidant exposures and micropollutant abatement during ozonation using a machine learning method, Environ. Sci. Technol. 55 (2021) 709–718.

[56] K. Lu, T. Ren, N. Yan, X. Huang, X. Zhang, Revisit the role of salinity in heterogeneous catalytic ozonation: the trade-off between reaction inhibition and mass transfer enhancement, Environ. Sci. Technol. (2023).

[57] P. Arathala, R.A. Musah, Oxidation of dipropyl thiosulfinate initiated by Cl radicals in the gas phase: implications for atmospheric chemistry, ACS Earth Space Chem. 5 (2021) 2878–2890.